

This is the accepted manuscript made available via CHORUS. The article has been published as:

## Origins of Extreme Liquid Repellency on Structured, Flat, and Lubricated Hydrophobic Surfaces

Dan Daniel, Jaakko V. I. Timonen, Ruoping Li, Seneca J. Velling, Michael J. Kreder, Adam Tetreault, and Joanna Aizenberg

Phys. Rev. Lett. **120**, 244503 — Published 15 June 2018

DOI: [10.1103/PhysRevLett.120.244503](https://doi.org/10.1103/PhysRevLett.120.244503)

# Origins of extreme liquid-repellency on structured, flat, and lubricated hydrophobic surfaces

Dan Daniel<sup>1,2,\*</sup>, Jaakko V. I. Timonen<sup>1,3</sup>, Ruoping Li<sup>4</sup>, Seneca J. Velling<sup>4</sup>,  
Michael J. Kreder<sup>1</sup>, Adam Tetreault<sup>4</sup>, and Joanna Aizenberg<sup>1,4,5†</sup>

<sup>1</sup>*John A. Paulson School of Engineering and Applied Sciences,  
Harvard University, Cambridge, MA 02138, USA*

<sup>2</sup>*Institute of Materials Research and Engineering, 2 Fusionopolis Way, Singapore 138634*

<sup>3</sup>*Department of Applied Physics, Aalto University School of Science, Espoo, FI-02150, Finland*

<sup>4</sup>*Wyss Institute for Biologically Inspired Engineering,  
Harvard University, Cambridge, MA 02138, USA and*

<sup>5</sup>*Kavli Institute for Bionano Science and Technology,  
Harvard University, Cambridge, MA 02138, USA*

There are currently three main classes of liquid-repellent surfaces: micro-/nano-structured superhydrophobic surfaces, flat surfaces grafted with ‘liquid-like’ polymer brushes, and lubricated surfaces. Despite recent progress, the mechanistic explanation for the differences in droplet behavior on such surfaces is still under debate. Here, we measured the dissipative force acting on a droplet moving on representatives of these surfaces at different velocities  $U = 0.01$ – $1$  mm/s using a cantilever force sensor with sub- $\mu$ N accuracy, and correlated it to the contact line dynamics observed using optical interferometry at high spatial (micron) and temporal ( $< 0.1$ s) resolutions. We find that the dissipative force—due to very different physical mechanisms at the contact line—is independent of velocity on superhydrophobic surfaces, but depends non-linearly on velocity for flat and lubricated surfaces. The techniques and insights presented here will inform future work on liquid-repellent surfaces and enable their rational design.

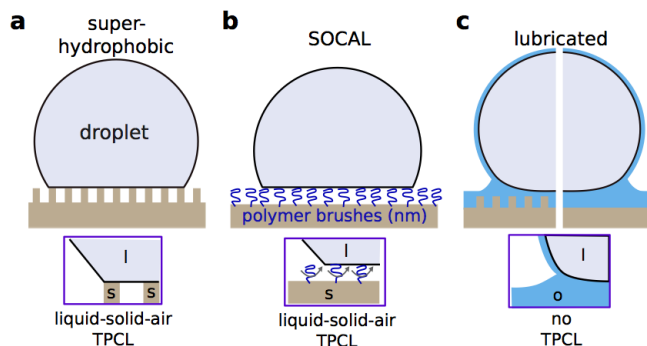


FIG. 1. Schematics of liquid-repellent surfaces. a, Structured superhydrophobic (SH) surfaces. b, Flat surfaces grafted with polymer brushes, dubbed Slippery Omniphobic Covalently Attached Liquid (SOCAL) surfaces. c, Structured (left) or flat (right) lubricated surfaces. The droplet is shown with a lubricant cloaking layer, which is typical for low-surface-tension lubricants (Supplementary Figure S1).

In Nature, the ability to repel water is often a matter of life and death. For example, insects must avoid getting trapped by falling raindrops and plants need to keep their leaves dry for efficient gas exchange through the stomata [1, 2]. Similarly, the tendency of water and complex fluids, such as blood and oil, to stick to surfaces pose many challenges to industries, ranging from contamination of biomedical devices to increased hydrodynamic

drag in ships [3, 4]. Hence, there is a huge interest in developing liquid-repellent materials. To achieve this, there are three main approaches. Firstly, hydrophobic micro-/nano-structures can be designed on the surface to maintain a stable air layer, minimizing contact between the liquid and the solid, i.e. lotus-effect superhydrophobic (SH) surfaces (Figure 1a) [3, 5]. Secondly, a flat surface can be grafted with nanometer-thick ‘liquid-like’ polymer brushes (Figure 1b); the resulting surface, dubbed Slippery Omniphobic Covalently Attached Liquid (SOCAL), is able to repel various liquids, including low-surface-tension alkanes [6–8]. Finally, a suitable lubricant oil can be added to the surface, which can be structured as is the case for Slippery Liquid-Infused Porous Surfaces (SLIPS) [9, 10] or flat as is the case of lubricant-infused organogels [11, 12] (Figure 1c); any liquid can then easily be removed, as long as there is a stable intercalated lubricant layer [13–16].

While each of the three surfaces has been studied separately, there have been few attempts to compare their relative liquid-repellent performance. In this Letter, we will elucidate the origin of liquid repellencies for the three surfaces and show how details of the liquid-solid-air three phase contact line (TPCL) at the droplet’s base—or the absence of TPCL in the case of lubricated surfaces—lead to different droplet dynamics.

Previous work generally reports the static apparent contact angle  $\theta_{\text{app}}$  and emphasizes the low contact angle hysteresis  $\Delta\theta = \theta_{\text{adv}} - \theta_{\text{rec}} < 10^\circ$ , where  $\theta_{\text{adv}}$ ,  $\theta_{\text{rec}}$  are the advancing and receding contact angles measured optically from the side (Table I and Supplementary Tables S1 and S2 for typical values) [17]. The low contact angle hysteresis translates to low dissipative force  $F_d$  acting on

\* daniel@imre.a-star.edu.sg

† jaiz@seas.harvard.edu

TABLE I. Reported contact angle values for a water droplet

Surface	$\theta_{\text{app}}$	$\Delta\theta$	$\Delta\cos\theta$
SOCAL	90–110°	1–10°	0.02–0.2
Lotus-effect	> 150°	2–10°	0.02–0.1
Lubricated	90–110°	1–5°	0.02–0.05

the droplet, since

$$F_d = 2a\gamma\Delta\cos\theta, \quad (1)$$

where  $\Delta\cos\theta = \cos\theta_{\text{rec}} - \cos\theta_{\text{adv}}$ , and  $a$  and  $\gamma$  are the base radius and the surface tension, respectively (Furmidge's relation) [17, 18]. However, for most studies, the exact experimental conditions—in particular, the speed of the contact line  $U$ —are often not controlled, even though  $\Delta\cos\theta$  (and therefore  $F_d$ ) can depend on  $U$  [19–23]. Moreover, there are other technical challenges:  $\theta$  is difficult to determine accurately when its value is too high > 170° (SH surfaces) [24, 25] or when obscured by a wetting ridge (lubricated surfaces) [16].

In this study, to avoid the ambiguity in interpreting contact angle measurements, we measured  $F_d$  for a droplet moving at controlled speed  $U$  directly using a cantilever force sensor (Figure 2) [14, 26, 27]. The droplet was attached to a capillary tube, and the force  $F_t(t)$  acting on the droplet was inferred from the tube's deflection  $\Delta x(t)$ :  $F = k\Delta x$ , where  $k = 5\text{--}25\text{ mN/m}$  for tube-lengths  $L = 6\text{--}9\text{ cm}$ . Note that the distortion to the droplet shape due to the tube is minimal (Supplementary Figure S2). Details of the custom-built setup can be found in our previous work [14].

Figure 2a shows the characteristic force curves for the three surfaces.  $F_d$  is taken to be the long-time average, once  $F_t$  has reached a steady state. Typically, a larger force  $F_{\text{peak}}$  is required to jumpstart the motion, reminiscent of the static and kinetic friction forces between two solid surfaces [27]. For a lotus-effect surface, this  $F_{\text{peak}} = 6.6\text{ }\mu\text{N}$  is sharp and distinct from the force  $F_d = 5.0 \pm 0.2\text{ }\mu\text{N}$  required to maintain the motion. In contrast, for lubricated and SOCAL surfaces,  $F_{\text{peak}}$  tends to be broader and less defined. At time  $t \approx 50\text{ s}$ , the droplet motion was stopped: for a lubricated surface with no contact line pinning, the cantilever returned to its original position; in contrast, for SOCAL and lotus-effect surfaces with a TPCL, the droplet was pinned and  $F_t$  did not return to zero, but instead reached a finite value  $F_{\text{min}}$ .

As  $U$  was varied in the range of 0.01–1 mm/s, we found that  $F_d(U)$  acting on a  $1\text{ }\mu\text{L}$  water droplet exhibits different functional forms for the different surfaces, suggesting different mechanistic origins of liquid-repellency (Figure 2b). Firstly, there is a minimum force required to move the droplet on SH and SOCAL surfaces,  $F_{\text{min}} = 4$  and  $5\text{ }\mu\text{N}$ , respectively; in contrast, for lubricated surfaces,  $F_{\text{min}} = 0$  (Note that  $F_{\text{min}}$  in Figures 2a and b are the same). Secondly,  $F_d$  is independent of  $U$  for SH surfaces (dash-dot line, Figure 2b), but has a non-linear dependence on  $U$  for SOCAL and lubricated surfaces (dashed

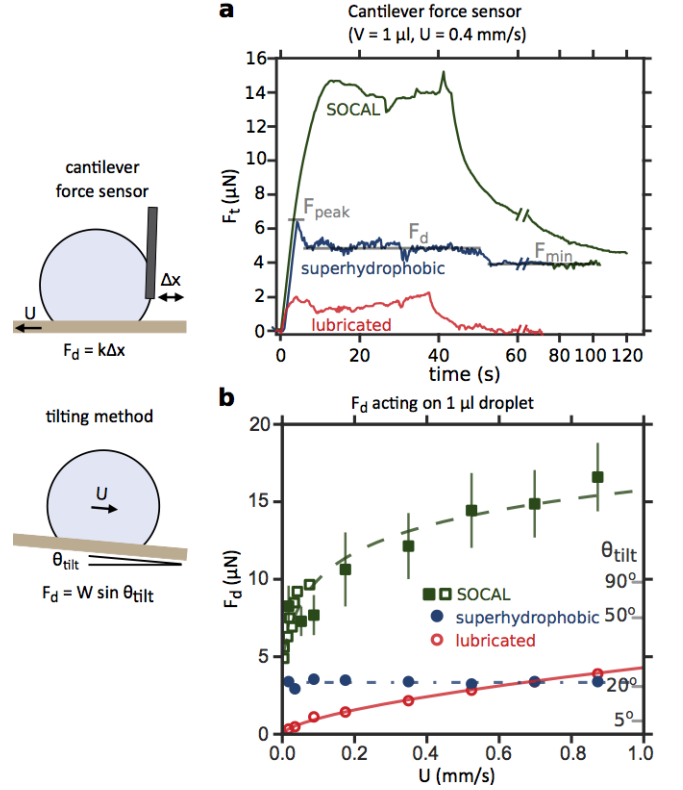


FIG. 2. a, Characteristic force curves for a water droplet moving on the three surfaces measured using a cantilever force sensor. The motor (to move the substrate) was started at time  $t = 0\text{ s}$  and stopped at  $t \approx 50\text{ s}$ . b,  $F_d$  for  $1\text{ }\mu\text{L}$  water droplets moving at speeds  $U = 0.01\text{--}1\text{ mm/s}$  on superhydrophobic (hexagonal array of micropillars with diameter  $d = 16\text{ }\mu\text{m}$ , pitch  $p = 50\text{ }\mu\text{m}$ , and height  $h_p = 30\text{ }\mu\text{m}$ ), SOCAL, and lubricated surfaces (filled circles, filled squares, and empty circles, respectively).  $U$  of droplets tilted at different  $\theta_{\text{tilt}} = 25\text{--}90^\circ$  on the same SOCAL surface and hence subjected to different  $F_d = W \sin \theta_{\text{tilt}}$  are shown on the same plot (empty squares).  $\Delta F_d < 0.2\text{ }\mu\text{N}$  for three repeats, unless otherwise indicated by error bars. See Supplementary Section S2 for details on sample preparation.

and solid lines, respectively). To validate the force sensor measurements, velocity data (open squares) of droplets sliding down the same SOCAL surface at different  $\theta_{\text{tilt}}$  are superimposed on the same plot.

These observations account for the qualitatively different droplet motion on a tilted surface. A  $10\text{ }\mu\text{L}$  water droplet was pinned on SH and SOCAL surfaces, when  $\theta_{\text{tilt}}$  is below a critical angle  $\theta_{\text{crit}} \approx 5^\circ$ ; above  $\theta_{\text{crit}}$ , at  $\theta_{\text{tilt}} = 15^\circ$ , the droplet accelerated at  $0.4\text{ m/s}^2$  on the SH surface, but moved at constant velocity  $U_{\text{const}} = 8\text{ mm/s}$  on the SOCAL surface (Figure 3a, b). Eventually, the accelerating droplet on the SH surface will reach a terminal velocity—likely due air drag—but at a much larger  $U_{\text{const}} \sim \text{m/s}$  [5]. In contrast, on lubricated surfaces, the droplet was never pinned and moved at increasing  $U$  with increasing  $\theta_{\text{tilt}}$  (Figure 3c).

To understand the origin and hence the functional form

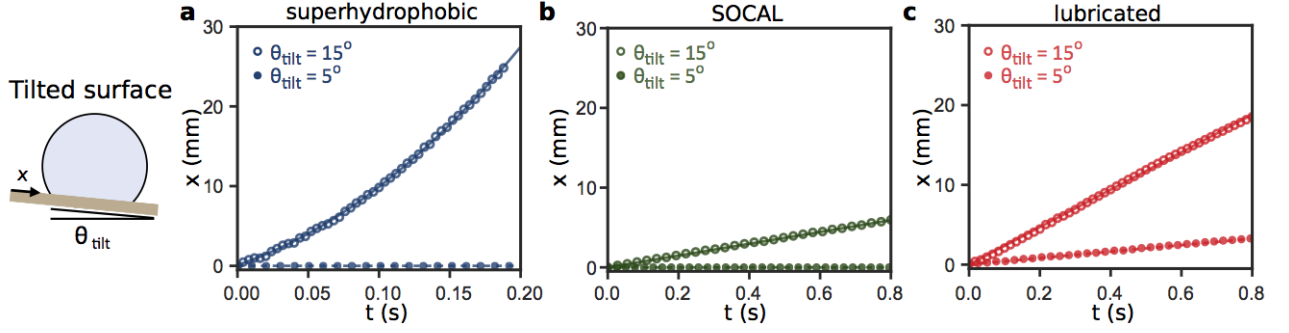


FIG. 3. Droplet motion on surfaces with  $\theta_{\text{tilt}} = 5^\circ$  and  $15^\circ$ . Depending on whether a droplet is moving with a constant speed or constant acceleration, the displacement  $x$  varies linearly or quadratically with  $t$ , respectively.

of  $F_d$ , we analyzed the base of moving droplets using reflection interference contrast microscopy (RICM) (Figure 4) [28]. We used a similar setup previously to study the lubricant dynamics of lubricated surfaces (supplementary Section S2) [14]. Using RICM, we were able to confirm the presence of a stable micron-thick air film beneath the droplet on a SH surface and to visualize the details of the contact line with much improved temporal and spatial resolutions compared to other techniques. For example, previous studies using confocal *fluorescence* microscopy usually require a dye to be added to the water droplet—which can affect its wetting properties—and can only achieve a temporal resolution of  $\Delta t$  of several seconds [29]. Environmental Scanning Electron Microscopy (SEM) can achieve sub-micron spatial resolution, but again with poor  $\Delta t$  of about 1s [30]. Moreover, the high-vacuum and low-temperature conditions of SEM may introduce artefacts and change the viscosity of the liquid(s), which in turn affect droplet behavior [14, 31].

Here, using RICM, we visualized the base of a droplet (without dye) moving on a transparent micropillar surfaces with a much improved  $\Delta t < 0.1$  s and good spatial details (Figure 4a-1). For example, the distortion of the receding contact line and the accompanying formation of capillary bridges can be observed unambiguously (Figure 4a-1,2); we were also able to capture details such as micro-droplets that are left behind after the break-up of the capillary bridges, which then evaporate away (Supplementary Figures S3 and S4, and Supplementary Movie S1). In contrast to the receding front, the advancing contact line was smooth and continuous (Figure 4a-3); most of the pinning therefore occurs at the receding front, consistent with previous reports [16, 32, 33].

We can estimate  $F_d$  by assuming that the force due to each pillar  $\sim \gamma d$  and the number of pillars in contact at the receding front  $\sim 2a/p$ :

$$F_d \sim (2a/p)\gamma d \approx 2a\gamma\phi^{1/2}, \quad (2)$$

where  $d$  and  $p$  are the pillars' diameter and pitch, and  $\phi$  is the solid surface fraction. We confirmed this scaling law experimentally, with each data point in Figure 4a representing SH surfaces of different  $\phi = 0.1$ – $0.4$  ( $d$

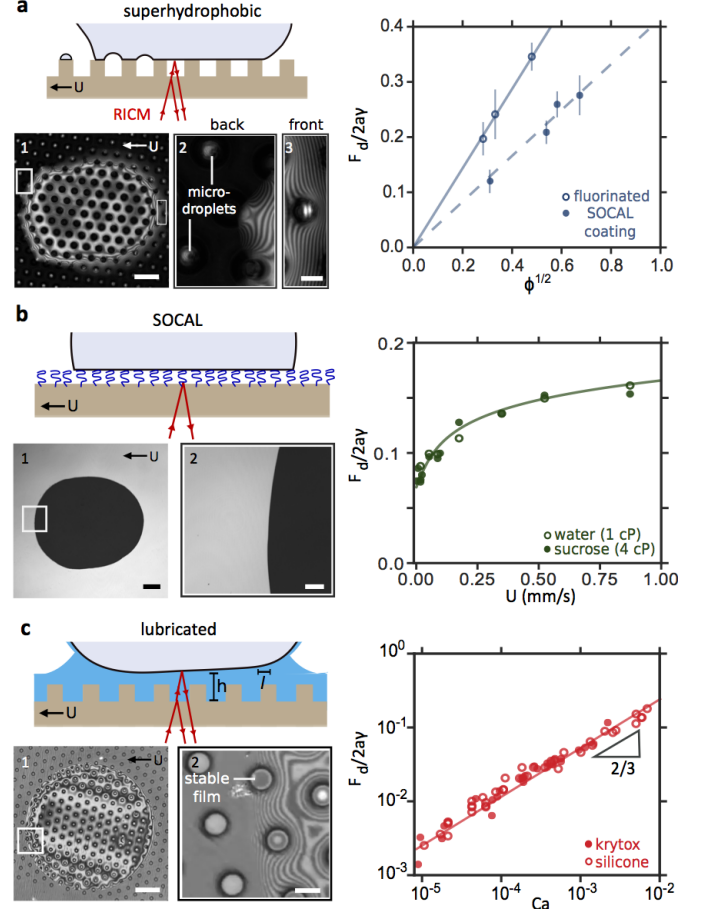


FIG. 4. Reflection interference contrast microscopy is used to visualize a) the intercalated air film on SH surface, b) the contact line on SOCAL surface, and c) the intercalated lubricant film on lubricated surfaces. Scale bars are 100  $\mu\text{m}$  for a-1, b-1, and c-1; 20  $\mu\text{m}$  for a-2,3 and c-2; and 30  $\mu\text{m}$  for b-2. The dissipative forces  $F_d$  are well-described by equations (2)–(4). Plots in a and b are generated from a much larger data set (Supplementary Figures S5 and S7). For b and c, the errors  $\Delta F_d/2a\gamma$  are  $10^{-2}$  and  $10^{-3}$ , respectively.

= 2–25  $\mu\text{m}$ ,  $p$  = 5–50  $\mu\text{m}$ , and  $h_p$  = 5–30  $\mu\text{m}$ ). The error bars in each data point is the standard deviation observed for water droplets (typically five or more) of volumes  $V$  = 0.5–8  $\mu\text{l}$  moving at  $U$  = 0.2–0.5 mm/s. The prefactor in equation (2) depends on the details of contact line distortion, which in turn depends on the surface functionalization; this explains the two different slopes observed in Figure 4a. The model described here, while simple, is able to account for the pinning force on SH surfaces reported here and elsewhere, at least as well as other models previously proposed in the literature (Supplementary Figures S5 and S6) [32, 34–36].

Using RICM, we were also able to visualize the unique features of the moving contact line on a SOCAL surface at  $U$  = 0.2 mm/s (Figure 4b). As was the case with SH surface, the shape of the contact line was elongated in the direction of motion, but unlike SH surface, the receding contact line is smooth without any visibly discrete pinning points (Figure 4b-1,2, cf. Figure 4a-1,2). The functional form of  $F_d$  for water and 30 wt% aqueous sucrose solution droplets moving at speeds  $U$  = 0.1–1 mm/s is consistent with Molecular-Kinetic Theory (MKT):

$$F_d = 2a\gamma[\Delta \cos \theta_o + 4K_B T / \gamma \xi^2 \operatorname{arcsinh}(U/2K_o \xi)]. \quad (3)$$

In MKT, the contact line motion is modeled as an absorption-desorption process, with a series of small jumps of size  $\xi$  and frequency  $K_o$ , while  $\Delta \cos \theta_o$  is  $\Delta \cos \theta$  in the limit of  $U \rightarrow 0$  (Supplementary Section S8) [19, 20]. Viscous dissipation is unimportant, and  $F_d$  is indistinguishable between water and 30 wt% sucrose droplets, despite their different viscosities,  $\eta$  = 1 and 4 cP, respectively [37].

Each data point in Figure 4b is an average of 3–5 droplets with volumes  $V$  = 1–5  $\mu\text{l}$ , while the line shows the best-fit curve, with  $\Delta \cos \theta_o$ ,  $\xi$  and  $K_o$  as fitting parameters. The values obtained for  $\xi$  = 3 nm and  $K_o$  = 7500  $\text{s}^{-1}$  are close to what were reported in the literature for other flat surfaces (Supplementary Table S3) [38, 39]. The value for  $\Delta \cos \theta_o$  = 0.07, on the other hand, is much lower than typically encountered. For example, a flat glass or silicon surface rendered hydrophobic by fluorosilanization typically has  $\theta_{\text{app}}$  = 110° and  $\Delta \theta$  = 15–30°, or equivalently  $\Delta \cos \theta_o$  = 0.3–0.5 [40]. The origin of the low  $\Delta \cos \theta_o$  on SOCAL surfaces was hypothesized to originate from the ability of polymer brushes to freely rotate at the moving contact line.

Interestingly, a combination of a SH and SOCAL surfaces, i.e. a micropillar surface coated with the same SOCAL polymer brush (filled circles, Figure 4a), behaves in a qualitatively different way from its flat SOCAL counterpart:  $F_d$  no longer depends on  $U$ , and scales with equation (2) rather than equation (3). Once again, this confirms that the pinning-depinning process at the micro-structured surface is fundamentally different from its chemically analogous flat surface.

For lubricated surfaces, there is no contact line pinning and hence the droplet base is circular in shape and not elongated (Figure 4c-1,2, cf. Figure 4a-1,2 and Figure

4b-1,2). The entrainment of lubricant generates a hydrodynamic lift force, and the droplet levitates over the surface with a film-thickness given by the Landau-Levich-Dejaguin law, i.e.  $h \sim RCa^{2/3}$ , where  $Ca = \eta_o U / \gamma_{lo}$  is the capillary number,  $\eta_o$  is the viscosity of the lubricant oil, and  $\gamma_{lo}$  is the liquid droplet-lubricant-oil interfacial tension [14, 41].  $F_d$  is dominated by the viscous dissipation at the rim of the droplet’s base of size  $l \sim RCa^{1/3}$ , and is therefore given by:

$$F_d \sim (\eta U / h) 2al \approx 2a\gamma_{lo} Ca^{2/3}. \quad (4)$$

This was experimentally verified for droplets of  $V$  = 1–5  $\mu\text{l}$  moving at  $U$  = 0.01–5 mm/s, with silicone/fluorinated oil of  $\eta$  = 5–60 cP as lubricants [14]. Note that this discussion is true only in the absence of solid-droplet contact; if for some reason, the lubricant film becomes unstable,  $F_d$  becomes dominated by contact line pinning and is independent of  $U$ , reminiscent of SH surfaces (Supplementary Figure S8).

TABLE II. Nature of contact angle hysteresis

Surface	$F_d/2a\gamma$ or $\Delta \cos \theta$	Comments
superhydrophobic	$\sim \phi^{1/2}$	no dependence on $U$
SOCAL	$\Delta \cos \theta_o + 4K_B T / \gamma \xi^2 \operatorname{arcsinh}(U/2K_o \xi)$	$\Delta \cos \theta \rightarrow \Delta \cos \theta_o$ , $U \rightarrow 0$
lubricated	$\sim Ca^{2/3}$	$\Delta \cos \theta \rightarrow 0$ , $U \rightarrow 0$

Comparing equations (2)–(4) with equation (1), we can get an expression for the dimensionless force per unit length  $F_d/2a\gamma$ , which is equivalent to the more conventional (but more ambiguous)  $\Delta \cos \theta$ , for the different surfaces, as summarized in Table II:  $\sim \phi^{1/2}$  for SH surfaces,  $\Delta \cos \theta_o + 4K_B T / \gamma \xi^2 \operatorname{arcsinh}(U/2K_o \xi)$  for SOCAL surfaces, and  $\sim (\gamma_{lo}/\gamma) Ca^{2/3} \approx Ca^{2/3}$  for lubricated surfaces. Recently, there has been some debate on the correct physical interpretation of contact angle hysteresis for lubricated surfaces [14, 16, 42]. We will address this more fully in a future publication, but in general  $\Delta \cos \theta \sim Ca^{2/3}$  corresponds to optical measurements of macroscopic  $\cos \theta_{\text{rec}} - \cos \theta_{\text{adv}}$ , and Furmidge’s relation can still be applied with some modifications (Supplementary Figure S9).

In summary, we have clarified the physics behind the three classes of liquid-repellent surfaces, in particular highlighting their distinct and unique properties, which are not captured by conventional contact angle measurements. We measured the dissipation force  $F_d$  with sub- $\mu\text{N}$  accuracy, and explicitly showed how the different functional forms of  $F_d$  (and hence the corresponding contact angle hysteresis) arise from details of the contact line. While we have confined our discussion to liquid-repellency, many of the ideas and techniques outlined here are relevant to various other problems, ranging from ice-repellency to the rational design of non-fouling materials.

## ACKNOWLEDGMENTS

The work was supported by the Office of Naval Research, U.S. Department of Defense, under MURI Award No. N00014-12-1-0875. J.V.I.T. was supported by the European Commission through the Seventh Framework Programme (FP7) project DynaSLIPS (project number

626954). This work was performed in part at the Harvard University Center for Nanoscale Systems (CNS), a member of the National Nanotechnology Coordinated Infrastructure Network (NNCI), which is supported by the National Science Foundation under NSF ECCS award no. 1541959. We acknowledge the use of the facilities at the Harvard Materials Research Science and Engineering Center (MRSEC) under award no. DMR-1420570.

- 
- [1] W. K. Smith and T. M. McClean, *Am. J. Bot.* **76**, 465 (1989).
  - [2] T. Darmanin and F. Guittard, *Mater. Today* **18**, 273 (2015).
  - [3] D. Quéré, *Annu. Rev. Mater. Res.* **38**, 71 (2008).
  - [4] L. Bocquet and E. Lauga, *Nat. Mat.* **10**, 334 (2011).
  - [5] M. Reyssat, D. Richard, C. Clanet, and D. Quéré, *Faraday Discuss.* **146**, 19 (2010).
  - [6] J. W. Krumpfer and T. J. McCarthy, *Faraday Discuss.* **146**, 103 (2010).
  - [7] D. F. Cheng, C. Urata, M. Yagihashi, and A. Hozumi, *Angew. Chem.* **51**, 2956 (2012).
  - [8] L. Wang and T. J. McCarthy, *Angew. Chem.* **128**, 252 (2016).
  - [9] A. Lafuma and D. Quéré, *Euro. Phys. Lett.* **96**, 56001 (2011).
  - [10] T.-S. Wong, S. H. Kang, S. K. Tang, E. J. Smythe, B. D. Hatton, A. Grinthal, and J. Aizenberg, *Nature (London)* **477**, 443 (2011).
  - [11] C. Urata, G. J. Dunderdale, M. W. England, and A. Hozumi, *J. Mater. Chem. A* **3**, 12626 (2015).
  - [12] J. Cui, D. Daniel, A. Grinthal, K. Lin, and J. Aizenberg, *Nat. Mater.* **14**, 790 (2015).
  - [13] J. D. Smith, R. Dhiman, S. Anand, E. Reza-Garduno, R. E. Cohen, G. H. McKinley, and K. K. Varanasi, *Soft Matter* **9**, 1772 (2013).
  - [14] D. Daniel, J. V. Timonen, R. Li, S. J. Velling, and J. Aizenberg, *Nat. Phys.* **13**, 1020 (2017).
  - [15] A. Keiser, L. Keiser, C. Clanet, and D. Quéré, *Soft Matter* **13**, 6981 (2017).
  - [16] F. Schellenberger, J. Xie, N. Encinas, A. Hardy, M. Klappper, P. Papadopoulos, H.-J. Butt, and D. Vollmer, *Soft Matter* **11**, 7617 (2015).
  - [17] P.-G. De Gennes, F. Brochard-Wyart, and D. Quéré, *Capillarity and wetting phenomena: drops, bubbles, pearls, waves* (Springer Science & Business Media, 2013).
  - [18] C. Furmidge, *J. Colloid Sci.* **17**, 309 (1962).
  - [19] J. H. Snoeijer and B. Andreotti, *Annu. Rev. Fluid Mech* **45**, 269 (2013).
  - [20] T. D. Blake, *J. Colloid Interface Sci.* **299**, 1 (2006).
  - [21] E. Bormashenko, Y. Bormashenko, and G. Oleg, *Langmuir* **26**, 12479 (2010).
  - [22] E. Bormashenko, *Colloid Polym. Sci.* **291**, 339 (2013).
  - [23] R. Tadmor, P. Bahadur, A. Leh, H. E. Nguessan, R. Jaini, and L. Dang, *Phys. Rev. Lett.* **103**, 266101 (2009).
  - [24] S. Srinivasan, G. H. McKinley, and R. E. Cohen, *Langmuir* **27**, 13582 (2011).
  - [25] J. T. Korhonen, T. Huhtamäki, O. Ikkala, and R. H. Ras, *Langmuir* **29**, 3858 (2013).
  - [26] D. Pilat, P. Papadopoulos, D. Schaffel, D. Vollmer, R. Berger, and H.-J. Butt, *Langmuir* **28**, 16812 (2012).
  - [27] N. Gao, F. Geyer, D. W. Pilat, S. Wooh, D. Vollmer, H.-J. Butt, and R. Berger, *Nat. Phys.* **14**, 191 (2018).
  - [28] J. de Ruiter, F. Mugele, and D. van den Ende, *Phys. Fluids* **27**, 012104 (2015).
  - [29] F. Schellenberger, N. Encinas, D. Vollmer, and H.-J. Butt, *Phys. Rev. Lett.* **116**, 096101 (2016).
  - [30] K. Smyth, A. Paxson, H.-M. Kwon, and K. Varanasi, *Surf. Innovations* **1**, 84 (2013).
  - [31] D. Richard and D. Quéré, *Europhys. Lett.* **48**, 286 (1999).
  - [32] M. Reyssat and D. Quéré, *J. Phys. Chem. B* **113**, 3906 (2009).
  - [33] L. Gao and T. J. McCarthy, *Langmuir* **22**, 6234 (2006).
  - [34] C. W. Extrand, *Langmuir* **18**, 7991 (2002).
  - [35] J. Joanny and P.-G. de Gennes, *J. Chem. Phys.* **81**, 552 (1984).
  - [36] H.-J. Butt, N. Gao, P. Papadopoulos, W. Steffen, M. Kappl, and R. Berger, *Langmuir* (2016).
  - [37] The force due to viscous dissipation can be estimated by noting that  $F_d U = \eta \int_V (\nabla U)^2 dV \approx \eta (U/R)^2 R^3$ , i.e.  $F_d \sim \eta U R \sim \text{nN}$ .
  - [38] S. R. Ranabothu, C. Karnezis, and L. L. Dai, *J. Colloid Interface Sci.* **288**, 213 (2005).
  - [39] R. A. Hayes and J. Ralston, *Langmuir* **10**, 340 (1994).
  - [40] D. Quéré, M.-J. Azzopardi, and L. Delattre, *Langmuir* **14**, 2213 (1998).
  - [41] L. Landau and V. Levich, *Acta Physicochim. USSR* **17**, 42 (1942).
  - [42] C. Semprebon, G. McHale, and H. Kusumaatmaja, *Soft matter* **13**, 101 (2017).
  - [43] See Supplemental Material [url] for the details of the experimental setup and theoretical analysis, which includes Refs. [44-52].
  - [44] B. Pokroy, A. K. Epstein, M. Persson-Gulda, and J. Aizenberg, *Adv. Mater.* **21**, 463 (2009).
  - [45] D. S. Bodas, A. Mandale, and S. Gangal, *Appl. Surf. Sci.* **245**, 202 (2005).
  - [46] P. Roach, N. J. Shirtcliffe, and M. I. Newton, *Soft Matter* **4**, 224 (2008).
  - [47] J. T. Simpson, S. R. Hunter, and T. Aytug, *Rep. Prog. Phys.* **78**, 086501 (2015).
  - [48] C. Urata, D. F. Cheng, B. Masheder, and A. Hozumi, *RSC Adv.* **2**, 9805 (2012).
  - [49] C. Urata, B. Masheder, D. F. Cheng, and A. Hozumi, *Langmuir* **29**, 12472 (2013).
  - [50] P. Kim, T.-S. Wong, J. Alvarenga, M. J. Kreder, W. E. Adorno-Martinez, and J. Aizenberg, *ACS Nano* **6**, 6569 (2012).
  - [51] A. Stalder, G. Kulik, D. Sage, L. Barbieri, and P. Hoffmann, *Colloids Surf., A* **286**, 92 (2006).
  - [52] G. McHale, N. J. Shirtcliffe, and M. I. Newton, *Langmuir*

**20**, 10146 (2004).